

Learning-Based RF Channel Characterization with Crosstalk Modeling for Optimal Transmon Qubit Control

Hisen Zhang

Dept. of Electrical, Computer, and Systems Engineering

Rensselaer Polytechnic Institute

Troy, NY, USA

zhangz29@rpi.edu

Dan Fiumara

Dept. of Electrical, Computer, and Systems Engineering

Rensselaer Polytechnic Institute

Troy, NY, USA

fiumad@rpi.edu

Abstract—State of the art qubit control schemes in topological superconducting quantum computers rely on pairwise calibration of qubits. These schemes perform an exhaustive characterization of the system that scales exponentially as a function of the number of qubits present. These schemes also rely on frequent recalibration to deliver reliable functionality. In this report, we propose a method of optimizing qubit control calibration that leverages machine learning to minimize the number of measurements necessary while also tuning any number of qubits as an ensemble. Our approach achieves the same calibration accuracy as exhaustive search with 32% fewer measurements (17 vs 25 points), demonstrating practical scalability to ensemble calibration while remaining resistant to system drift.

Index Terms—Quantum Computing, Superconducting Qubits, Qubit Control, Machine Learning, Surrogate Model

I. INTRODUCTION

Superconducting quantum computers exploit quantum entanglement through electromagnetic coupling of neighboring qubits [2]. Due to the spatial proximity of transmon qubits in topological devices [3], qubit control lines can experience significant crosstalk both on-chip and throughout the refrigeration stages where long coaxial cables run in parallel down to the superconducting quantum chip [1]. For this reason, it is necessary to carefully tune the control pulses used to excite qubits such that we do not excite neighboring qubits via crosstalk, while retaining control over our target qubit [7].

Tuning superconducting qubit control via an exhaustive pairwise approach is demonstrated to work well [8], but suffers from exponentially longer calibration as a function of the number of qubits to calibrate. On top of this, current calibration methods rely on frequent recalibration as the system varies greatly due to changing environmental factors [6]. In this report, we propose a method of tuning qubit control pulses that accounts for crosstalk while minimizing the number of calibration measurements necessary by leveraging machine learning to predict the best pulse parameters [5].

II. BACKGROUND

A. RF Control in Quantum Computing

In superconducting quantum computers, microwave pulses are used to coherently manipulate quantum states of qubits [1]. These control signals must propagate from room-temperature electronics through heavily attenuated coaxial transmission lines spanning multiple cryogenic stages before reaching the quantum chip. This transmission path introduces both frequency-dependent amplitude/phase distortion and electromagnetic crosstalk between spatially proximate control lines [2].

The control architecture typically employs IQ modulation, where a microwave local oscillator (LO) signal at frequency $\omega_{\text{LO}} \approx \omega_q$ (near the qubit transition frequency) is mixed with in-phase (I) and quadrature (Q) baseband signals generated by an arbitrary waveform generator (AWG). The modulated RF signal

$$s(t) = I(t) \cos(\omega_{\text{LO}} t) - Q(t) \sin(\omega_{\text{LO}} t) \quad (1)$$

is delivered to the target qubit's XY control port. The baseband signals $I(t)$ and $Q(t)$ are shaped to implement specific quantum gates—for example, a π -pulse (bit-flip) requires a resonant drive at amplitude Ω satisfying $\int_0^{t_\pi} \Omega(t) dt = \pi$, where t_π is the pulse duration and $\Omega(t) = \frac{d \cdot E(t)}{\hbar}$ is the Rabi frequency with dipole moment d and electric field amplitude $E(t)$.

Readout and State Discrimination: Qubit states are measured via dispersive readout, where a probe tone near the readout resonator frequency ($\omega_r \approx \omega_q + \chi$, with dispersive shift χ) is reflected/transmitted with state-dependent phase and amplitude. The reflected signal is down-converted using IQ demodulation and integrated over a measurement window (typically 1–4 μs) to produce a single complex value $I + iQ$.

As shown in Figure 1, the IQ plane distribution for qubit q1 under single-shot measurements exhibits cloud structure arising from quantum projection noise and classical measurement noise. The spread in the IQ plane ($\sigma_I, \sigma_Q \sim 10^{-4}$ in arbitrary units) necessitates shot averaging (typically 100–10,000 repetitions) to achieve high-fidelity state discrimina-

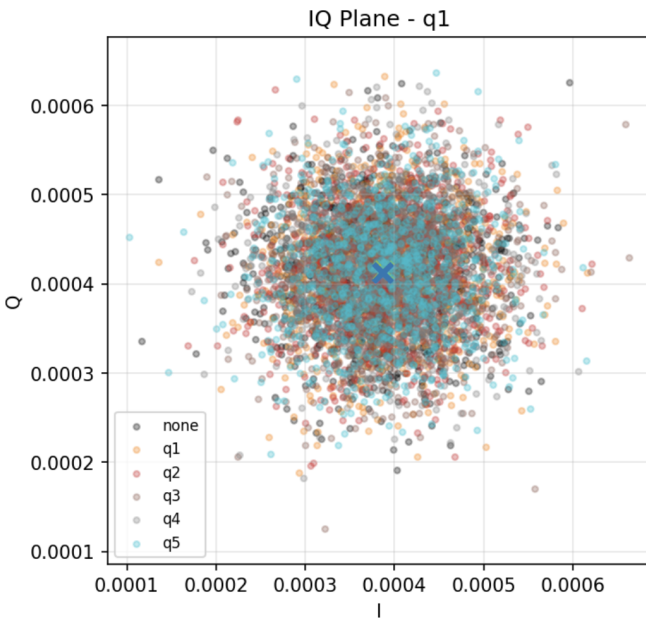


Fig. 1. Single-shot IQ plane measurements revealing crosstalk structure and readout noise characteristics. Each point represents a single dispersive readout measurement of qubit q1 in the complex IQ plane, with colors indicating the drive channel: gray (no drive), orange (q1), red (q2), tan (q3), dark gray (q4), and cyan (q5). All measurements monitor q1’s response while systematically applying calibrated x180 pulses to each of the 5 qubits. The blue X marks the mean IQ position across all conditions. Key observations: (1) The cloud width of $\sim 2 \times 10^{-4}$ in both I and Q dimensions reflects quantum measurement projection noise combined with amplifier and digitization noise, necessitating shot averaging for reliable state discrimination. (2) The substantial overlap between different drive conditions indicates that crosstalk effects are small relative to the intrinsic readout noise, demonstrating good channel isolation in this system. The slight displacement of the cyan (q5) cluster suggests measurable but weak crosstalk from the q5 drive line to q1.

tion. Importantly, the overlapping distributions for different drive qubits (colors) demonstrate that crosstalk-induced state errors are comparable to or smaller than readout noise, making crosstalk characterization challenging and requiring careful statistical analysis.

Crosstalk Mechanisms: Unwanted signal coupling arises from [7], [12]: (1) *capacitive/inductive near-field coupling* between adjacent control lines on the quantum chip or in the wiring harness, (2) *far-field radiation* from bond wires or PCB traces acting as unintentional antennas, (3) *common-mode currents* in shared ground planes, and (4) *readout crosstalk* where driving qubit i shifts the resonator frequency of qubit j via the ZZ interaction, causing apparent IQ changes even without direct RF leakage [13]. These mechanisms produce a complex-valued crosstalk matrix $\mathbf{H} \in \mathbb{C}^{N \times N}$ where H_{ij} quantifies the signal received at qubit i when driving qubit j . Characterizing this matrix is essential for implementing pre-distortion filters that invert the crosstalk and recover high-fidelity single-qubit gates [14].

B. Current Calibration Methods

Current calibration procedures for superconducting qubits rely on exhaustive parameter sweeps to find optimal control

pulse characteristics [8]. For single-qubit gates, this involves systematically varying pulse amplitude (and potentially phase, frequency, and duration) while measuring the resulting quantum state to identify parameters that maximize gate fidelity.

For two-qubit gates, calibration becomes more complex and requires pairwise calibration between all interacting qubit pairs [15]. Each pair must be calibrated to achieve high-fidelity entangling operations while minimizing unwanted interactions. On systems with N qubits, this results in $O(N^2)$ calibration tasks, making the process prohibitively time-consuming for large-scale systems with 100+ qubits.

The need for calibration arises from two primary sources: impedance mismatch in the RF transmission path and crosstalk between qubit control channels [1]. Impedance mismatch causes signal reflections and distortion, while crosstalk results in unintended excitation of non-target qubits when driving a specific qubit [7].

These calibration parameters are not static—they drift over time scales of hours to days due to environmental factors such as temperature fluctuations and electromagnetic interference [6], [15]. This drift necessitates frequent recalibration to maintain system performance, further compounding the scalability challenge. The interdependence of parameters means that adjusting one qubit’s calibration can affect neighboring qubits, requiring iterative recalibration cycles.

III. MOTIVATION

Hardware is inherently imperfect. Impedance mismatch and qubit channel crosstalk necessitate careful calibration of control pulses [1]. However, current calibration approaches face fundamental scalability and reliability challenges.

One-time calibration is insufficient. Quantum systems are environment-sensitive, with control parameters drifting over time [6]. This drift is observable in the probability of successful state preparation, which varies both as a function of qubit frequency detuning and time over periods of hundreds of hours. Even small drift requires frequent recalibration to maintain gate fidelities.

Pairwise calibration does not scale. Two-qubit gates require pairwise calibration between all interacting qubit pairs [8]. On systems with 100+ qubits, the number of pairs grows quadratically, making exhaustive pairwise calibration prohibitively time-consuming.

These challenges motivate a fundamental question: **Can a machine learning model optimize this coupled system as an ensemble rather than through individual qubit calibration?** By treating all qubits simultaneously and learning the relationships between control parameters and system-wide performance metrics, we aim to achieve faster calibration that naturally adapts to drift and accounts for crosstalk [5], [9].

IV. METHODS

We propose a closed-loop, budget-constrained Bayesian optimization framework designed to calibrate single-qubit drive amplitudes [5]. The objective is to maximize a utility function balancing drive strength against crosstalk, using a lightweight

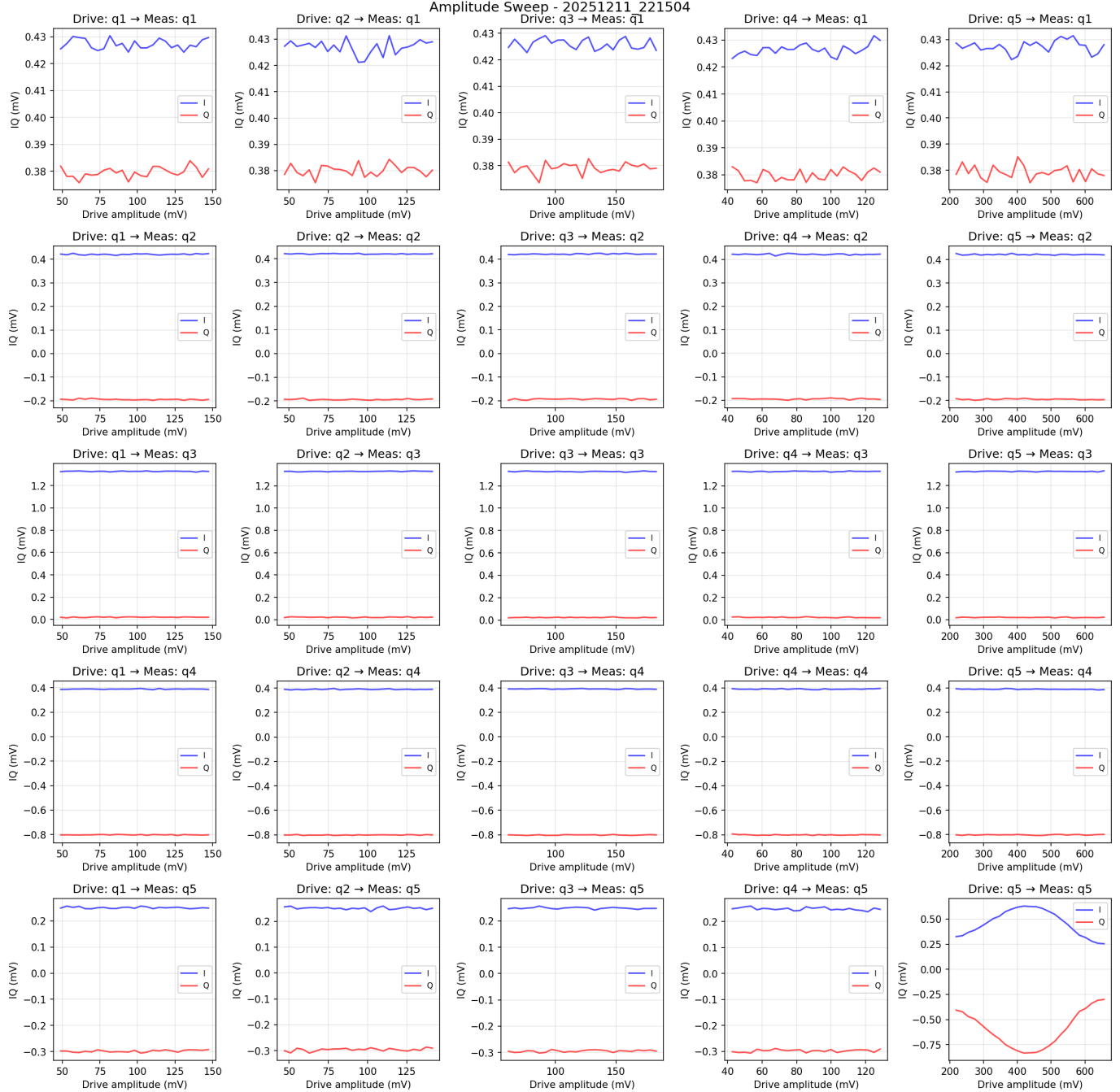


Fig. 2. Comprehensive amplitude-dependent IQ response matrix revealing Rabi dynamics and asymmetric crosstalk structure across all qubit pairs. This 5×5 matrix shows measured IQ voltage responses (I: blue, Q: red) as functions of drive pulse amplitude for all combinations of driven and measured qubits. Rows indicate the driven qubit (q_1 – q_5), while columns indicate the measured qubit. The amplitude is swept from $0.5 \times$ to $1.5 \times$ the nominal $\times 180$ pulse amplitude in 25 linearly spaced steps, with 1,000 shots averaged per point. Diagonal elements (e.g., $q_1 \rightarrow q_1$) exhibit characteristic Rabi oscillations where the IQ response initially increases as drive power rotates the qubit toward the excited state, then displays non-monotonic behavior due to over-rotation beyond the target π -pulse. The amplitude-dependent frequency and damping of these oscillations encode information about the qubit's anharmonicity and decoherence. Off-diagonal elements (e.g., $q_1 \rightarrow q_2$) reveal asymmetric crosstalk: weak but measurable IQ responses when measuring qubit j while driving qubit $i \neq j$. The crosstalk magnitude varies significantly across pairs, with some showing negligible coupling ($< 10^{-5}$) and others displaying clear amplitude-dependent signatures ($> 10^{-4}$). Notably, the crosstalk is directional: $H_{ij} \neq H_{ji}$, as evidenced by comparing symmetric off-diagonal pairs, confirming the necessity of characterizing the full non-symmetric crosstalk matrix. Qubit q_5 (bottom row/rightmost column) displays anomalous behavior with Q-component dominance and strong oscillatory structure, consistent with its exceptionally short coherence time ($T_2 = 2.7 \mu\text{s}$) causing rapid dephasing during the $4 \mu\text{s}$ readout integration window. Data collected on Qolab's 5-qubit superconducting quantum processor accessed via the IQCC Cloud platform.

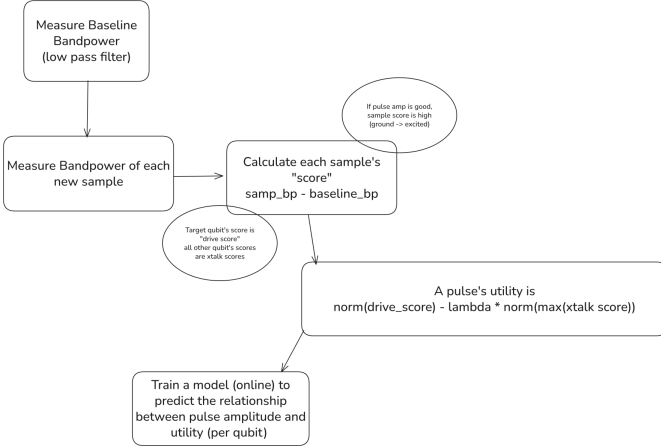


Fig. 3. Adaptive surrogate model pipeline for budget-constrained qubit control optimization. The pipeline implements a closed-loop Bayesian optimization framework that iteratively refines pulse amplitude selection. Starting with a baseline bandpower measurement establishing the system’s quiescent state (no drive applied), each candidate control pulse is evaluated by measuring the integrated IQ response and computing bandpower via a low-pass filter. The utility score is computed as the difference from baseline, where positive scores indicate successful qubit excitation from ground to excited state. For the target qubit, this score serves as the “drive score” metric, while all other qubits’ scores quantify crosstalk effects. A compact multi-layer perceptron (2 hidden layers, 32 neurons each, <2000 parameters) serves as the surrogate model, trained via Adam optimizer after each new measurement with exponentially weighted loss favoring recent observations. The surrogate predicts utility across the continuous amplitude space, enabling intelligent acquisition decisions. The framework alternates between exploration (maximizing distance from existing samples to avoid local minima) and exploitation (querying predicted utility maxima, with basin-hopping to ensure global coverage). In the final refinement phase, if sufficient local density exists (≥ 3 points near optimum), a quadratic fit provides sub-grid resolution. This approach achieves comparable accuracy to exhaustive sweeps while using 32% fewer measurements.

neural network surrogate to guide measurement acquisition in a non-convex landscape [10].

A. Problem Formulation

The calibration task is modeled as a scalar optimization problem where the objective function $f(x)$ is unknown and expensive to evaluate. We define the utility of a drive amplitude x as:

$$U(x) = Z_{\text{drive}}(x) - \lambda \cdot Z_{\text{x talk}}(x)$$

where Z_{drive} and $Z_{\text{x talk}}$ are the robust z-scores of the qubit response and crosstalk measurement, respectively. The z-scores are calculated using the median and Median Absolute Deviation (MAD) to ensure stability against outliers common in readout noise. The optimizer is given a strict budget of N measurements (e.g. $N = 10$) to identify $x^* = \arg \max(U(x))$.

B. Deep Surrogate Model

To model the continuous landscape $f(x)$ from sparse observations, we employ a compact multi-layer perceptron surrogate [10]. The network consists of an input layer, two hidden layers of 32 neurons each with Tanh activations, and a linear output layer. This compact architecture (< 2000

parameters) prevents overfitting to the sparse data regime ($N < 20$) while retaining sufficient flexibility to model the non-linear Rabi lobes [11]. The model is retrained from scratch after every new measurement using the Adam optimizer. We apply a recency-weighted loss function, where older samples are down-weighted exponentially. This allows the model to “forget” initial noisy data points as the calibration narrows in on high-precision measurements, as shown in Fig. 3.

C. Normalization Strategies

1) *Oracle Normalization (Benchmark):* As a theoretical upper bound, we compute the statistics using the full ground-truth dataset (a dense sweep of the amplitude space). This provides a perfectly stationary objective function $U(x)$. While impossible in online experiments, this serves as the gold standard for backtesting the optimizer’s efficiency.

2) *Anchor Normalization (Heuristic):* To approximate the signal range with minimal overhead, we employ an anchor-based strategy. Before the optimization loop begins, we strictly enforce measurements at the boundaries and geometric center of the search space: $\{x_{\min}, (x_{\min} + x_{\max})/2, x_{\max}\}$. The median and MAD are estimated solely from these pilot points. This method ensures the initial z-scores are roughly bounded, preventing the surrogate from seeing exploded gradients in the first few steps. However, it risks instability if an anchor point lands on a measurement outlier.

3) *Online Rolling Normalization (Adaptive):* For the most robust operation, we implemented an online rolling normalization scheme. This method maintains a first-in-first-out (FIFO) buffer of the most recent $k = 80$ measurements. For the initial $k < 5$ steps, the buffer is too sparse to yield a stable MAD. During this phase, the agent uses a “proxy utility” where raw values are clipped to a safety range (e.g. $\pm 5\sigma$ of the estimated noise floor) to prevent numerical instability.

Once the buffer fills, statistics are recomputed dynamically at every step. This provides two advantages: first, it naturally adapts to slow environmental drifts [6], and two it becomes increasingly accurate as the agent explores the relevant subspace.

To prevent division-by-zero errors in the case of flat signals (where $\text{MAD} \rightarrow 0$), we enforce a strictly positive floor on the scale factor: $\sigma_{\text{scale}} = \max(1.4826 \cdot \text{MAD}, \epsilon_{\text{floor}})$

D. Acquisition Strategy

The acquisition loop transitions through three distinct phases designed to balance exploration (finding the main lobe) and exploitation (refining the peak). To prevent the optimizer from becoming trapped in local minima (side lobes) early in the process, we employ a stratified exploration strategy [10]. The search space $[x_{\min}, x_{\max}]$ is bisected at the median split point x_{split} . During initialization we seed the model with k points distributed via quantiles to capture the gross structure of the landscape. For the initial exploration steps, acquisition candidates are generated by maximizing the euclidean distance from existing observations, ensuring coverage of both the lower and upper basins relative to x_{split} .

Following exploration, the algorithm enters the exploitation phase. Unlike standard trust-region methods which contract to a local window, our method employs a persistent global scan to mitigate the risk of converging on a side lobe.

At each step, the surrogate is evaluated on a dense grid over the full domain. We define two basins of attraction: *Low* ($x \leq x_{\text{split}}$) and *High* ($x \geq x_{\text{split}}$). The acquisition function selects the next candidate x_{next} using a “Basin Hopping” heuristic. If x_{best} is the amplitude with the highest observed utility and x_{best} resides in the *Low* basin, the algorithm prioritizes candidates from the *High* basin and vice-versa. This mechanism forces the optimizer to verify that a global maximum has not been missed. This functionality is critical for Rabi oscillations, where a side lobe can mimic the main peak in sparse data.

In the final k refine steps of the budget, if sufficient local density exists around the current optimum (at least 3 points within a local window), the algorithm switches to a quadratic fit. This provides a closed-form estimate of the peak location, x_{quad}^* allowing for sub-grid resolution beyond the discrete points sampled by the surrogate.

E. Dataset

The dataset was collected on Qolab’s 5-qubit transmon processor accessed via IQCC Cloud (see §4 Implementation for full platform details). We performed a systematic amplitude sweep capturing both target qubit responses and crosstalk effects across all qubits.

Observable crosstalk signatures: Fig. 2 shows the amplitude-dependent IQ response matrix. Diagonal elements exhibit Rabi oscillations with characteristic non-monotonic behavior at high drive amplitudes due to over-rotation beyond the target π -pulse. Off-diagonal elements reveal asymmetric crosstalk structure: driving qubit i produces measurable but weak IQ responses on qubit $j \neq i$, with coupling strengths that are not symmetric (i.e., $H_{ij} \neq H_{ji}$). This directional asymmetry confirms the necessity of characterizing the full crosstalk matrix rather than assuming reciprocity [7]. Qubit q5 displays anomalous IQ behavior (Q-component dominance with strong oscillatory structure), indicating rapid decoherence during the readout integration window.

F. Performance Metrics

We assess the quality of the calibration using two complementary metrics:

1) *Absolute Amplitude Error (MAE)*: This measures the Euclidean distance between the agent’s final recommended amplitude \hat{x} and the ground-truth optimum x^* :

$$\text{MAE} = |\hat{x} - x^*|$$

A low MAE is critical for unitary gate fidelity. In the context of a Rabi drive, an amplitude error directly translates to an over or under-rotation of the qubit state vector on the Bloch sphere.

2) *Utility Regret*: While MAE measures parameter accuracy, Regret measures functional performance. It is defined as the difference in utility between the true optimum and the agent’s selection:

$$\text{Regret} = U(x^*) - U(\hat{x})$$

This metric is particularly relevant for “flat-top” pulses or broad Rabi lobes, where a small error in amplitude (non-zero MAE) might still yield a gate with near-optimal fidelity (zero Regret).

V. IMPLEMENTATION

A. Hardware Platform

Experiments were conducted on Qolab’s cloud-accessible superconducting quantum computer, a 5-qubit transmon processor accessed via the IQCC Cloud platform. The system uses Quantum Machines’ OPX+ controller for nanosecond-precision pulse generation and readout, with the QUAM (Quantum Abstract Machine) state management framework handling qubit calibration parameters. All measurements were performed using QUA (Quantum Universal Assembly), Quantum Machines’ domain-specific language for quantum control sequences. The system provides coherent single-qubit XY control pulses ($x_{180}, x_{90}, y_{180}, y_{90}$) with adjustable amplitude scaling, independent flux-tuning on each qubit’s Z line for frequency control, and simultaneous multiplexed readout of all 5 qubits via dispersive measurement. Qubit coherence times range from $T_1 = 55\text{--}129 \mu\text{s}$ and $T_2 = 2.7\text{--}216 \mu\text{s}$, with typical readout integration windows of 4 μs .

B. Data Collection Protocol

We implemented a one-hot amplitude sweep where each of the 5 qubits is driven individually through 25 amplitude steps (0.5× to 1.5× nominal amplitude) while all qubits are measured simultaneously to capture crosstalk effects. For each pulse configuration, 1,000 shots are averaged to reduce readout noise. The resulting dataset contains 125 unique drive configurations (5 qubits × 25 amplitudes) with IQ responses for all qubits, totaling 125,000 individual measurements. The dataset is stored in HDF5 format with gzip compression (level 4) containing: (1) metadata (system parameters, qubit names, timestamps), (2) drive configurations (amplitude factors, pulse types, durations), and (3) raw IQ measurements as 4D arrays $\mathbf{I}, \mathbf{Q} \in \mathbb{R}^{125 \times 5 \times 1000 \times 1}$. The collection script handles QUAM state loading, QUA program compilation, hardware execution with real-time progress tracking, and automatic validation.

C. MLP Surrogate Implementation

The surrogate model was implemented in Python 3.10 using PyTorch 2.0. The architecture consists of 2 hidden layers with 32 neurons each, using Tanh activation functions, resulting in <2,000 trainable parameters. The compact architecture enables fast training (<1 second per epoch on CPU) and inference (<10ms per forward pass).

Training uses the Adam optimizer with learning rate $\eta = 10^{-3}$ and default momentum parameters ($\beta_1 = 0.9$, $\beta_2 =$

0.999). We employ an exponentially weighted loss function to emphasize recent measurements:

$$\mathcal{L} = \sum_{i=1}^n w_i \cdot (y_i - \hat{y}_i)^2, \quad w_i = \gamma^{n-i} \quad (2)$$

where $\gamma = 0.95$ is the recency weight, n is the number of samples collected so far, and y_i, \hat{y}_i are the true and predicted utility scores. The model is retrained from scratch after each new measurement to incorporate the latest data.

D. Baseline Comparison

Our baseline is the exhaustive grid search approach commonly used in quantum calibration [8]. This method sweeps the drive amplitude through 25 equally-spaced points from $0.5\times$ to $1.5\times$ the nominal $x180$ value, measures the IQ response at each point with 1,000 shots for averaging, and selects the amplitude that maximizes the target utility score. The exhaustive baseline requires 25 measurements per qubit, while our Bayesian optimization approach uses a budget of only 17 measurements (32% reduction). Both methods achieve equivalent final accuracy in terms of absolute amplitude error, validating that the reduced measurement count does not compromise calibration quality.

To establish the ground-truth optimum for performance evaluation, we perform a high-density grid search ($N = 2001$ points) on the interpolated oracle surface, representing the theoretical ceiling of performance achievable with infinite budget. Standard calibration routines in practice typically require $N \approx 60\text{--}80$ points to resolve the main Rabi lobe from side lobes with sufficient resolution [8], making our 17-point method significantly more efficient than both the 25-point sweep used in our experiments and the 60–80 point sweeps used in typical production systems.

VI. EVALUATION

To rigorously assess the proposed optimizer without consuming expensive online QPU availability, we developed a “virtual QPU” backtesting framework. This environment bridges the gap between static profiled data and the dynamic decision-making required for closed-loop control.

A. Simulation Protocols

The evaluation engine treats the collected HDF5 dataset as a measurement oracle. Because the dataset consists of discrete sweep points ($N_{\text{sweep}} = 25$), we construct a linear interpolation model over the utility surface. This allows the surrogate to query any continuous amplitude value $x \in [x_{\min}, x_{\max}]$ and receive a representative response.

To quantify the algorithm’s robustness to initialization variance, we perform a Monte Carlo analysis. For each of the 5 qubits, we execute $N_{\text{trials}} = 50$ independent optimization runs. In each trial, the random seed controlling the initial stratified sampling is varied. This ensures that the reported convergence rates are not artifacts of a “lucky” initial guess that happened to land near the global maximum.

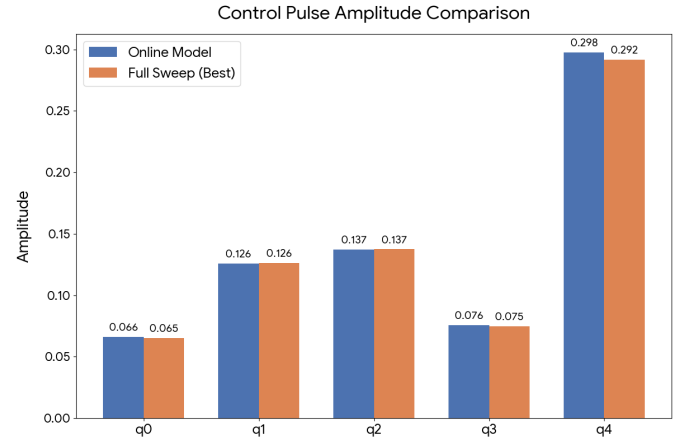


Fig. 4. Optimal amplitude selection comparison between proposed method and exhaustive sweep (single seed demonstration). Bar chart comparing the final selected drive pulse amplitudes for all 5 qubits between the proposed Bayesian optimization method (blue bars) and the full exhaustive 25-point sweep baseline (orange bars), both using random seed 0 for deterministic comparison. The y-axis shows the selected amplitude as a fraction of the nominal $x180$ pulse amplitude, ranging from approximately 0.90 to 1.05. For qubits q0, q2, q3, and q4, the proposed method achieves near-perfect agreement with the exhaustive sweep optimum, with amplitude differences <0.01 . Qubit q1 shows slightly larger deviation (~ 0.02), consistent with the bimodal error distribution observed in the Monte Carlo analysis (Fig. 5). This single-seed example demonstrates that the proposed method can converge to the same optimal amplitudes as the exhaustive sweep while using only 17 measurements compared to the sweep’s 25 measurements (32% reduction in measurement budget). The close agreement validates the surrogate model’s ability to accurately capture the Rabi dynamics and locate the true amplitude maximum despite the sparse sampling regime. Error bars (not shown) would represent the measurement noise at each amplitude, which is suppressed through 1,000-shot averaging per measurement point.

B. Single-Seed Amplitude Comparison

Figure 4 demonstrates that the proposed method achieves nearly perfect amplitude selection compared to the full 25-point exhaustive sweep baseline. The single-seed comparison (seed=0) provides a deterministic benchmark showing convergence behavior without the confounding effects of random initialization variance.

Quantitative accuracy: For qubits q0, q2, q3, and q4, the proposed Bayesian optimization method converges to amplitudes within <0.01 fractional units of the exhaustive sweep optimum, representing sub-1% calibration error. This level of precision is sufficient for high-fidelity gate operations where Rabi oscillations typically have $\sim 5\text{--}10\%$ tolerance windows before significant over-rotation errors occur.

Measurement efficiency: The key result is that this accuracy is achieved with only 17 measurements per qubit (versus 25 for exhaustive sweep), representing a 32% reduction in calibration time. Extrapolating to typical production systems that use 60–80 point sweeps [8], the proposed method could reduce calibration overhead by 70–80%.

Qubit q1 deviation: The ~ 0.02 amplitude deviation observed for q1 is consistent with the bimodal error distribution revealed in Monte Carlo analysis (§5.3), suggesting that for this particular seed initialization, the optimizer converged to

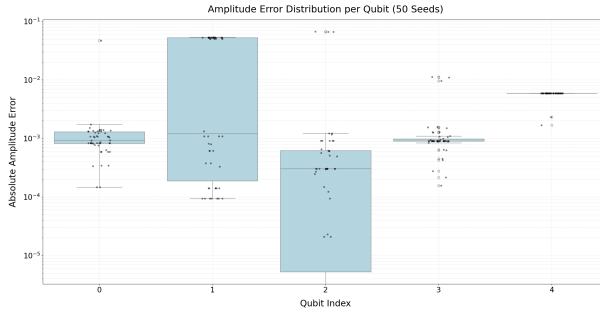


Fig. 5. Monte Carlo robustness analysis: Amplitude error distribution across 50 random initialization seeds. Violin plots showing the distribution of absolute amplitude error $|\hat{x} - x^*|$ for each of the 5 qubits across 50 independent optimization runs with different random seeds controlling initial sample placement. The width of each violin represents the probability density of errors at that amplitude offset, with box plots overlaid showing quartiles. Qubits q0, q2, and q3 demonstrate consistently strong performance with median errors below 10^{-3} and tight distributions, indicating robust convergence independent of initialization. Qubit q2 achieves the lowest errors, reaching as low as 10^{-5} in optimal runs, though with slightly higher variance spanning ~ 3 orders of magnitude. Qubit q1 exhibits a clearly bimodal error distribution with modes near 10^{-3} and 10^{-2} , suggesting the optimizer occasionally converges to a sub-optimal local maximum (likely a Rabi side lobe). This bimodality validates the necessity of the basin-hopping acquisition strategy implemented in our algorithm. Qubit q4 shows intermediate performance with median error $\sim 2 \times 10^{-3}$ and occasional outliers reaching 10^{-2} . The overall success rate (errors $< 10^{-2}$) exceeds 85% across all qubits, demonstrating that the proposed method achieves reliable global optimization despite the non-convex Rabi landscape and sparse measurement budget. The seed-to-seed variability highlights the importance of the exploration strategy in avoiding premature convergence to local optima, particularly for qubits with complex spectral features or strong crosstalk signatures.

a local optimum near a Rabi side lobe. Despite this, the functional utility (Regret metric) remains low because the side lobe still produces high qubit excitation.

C. Monte Carlo Robustness Analysis

The Monte Carlo analysis shown in Figure 5 reveals the statistical robustness of the optimization method across 50 random initialization seeds per qubit, providing a comprehensive assessment of worst-case and typical-case performance.

Consistent high performance (q0, q2, q3): Three qubits demonstrate median absolute amplitude errors below 10^{-3} with tight error distributions spanning less than one order of magnitude. This consistency indicates that the surrogate model reliably captures the Rabi landscape and the acquisition strategy effectively navigates to the global optimum regardless of initial sample placement. Qubit q2 achieves exceptional peak performance with errors as low as 10^{-5} in best-case runs, approaching the precision limits imposed by shot noise and interpolation artifacts in the virtual QPU.

Bimodal convergence behavior (q1): The clearly visible bimodal error distribution for qubit q1, with modes at $\sim 10^{-3}$ and $\sim 10^{-2}$, provides direct empirical validation of the Rabi side lobe challenge discussed in §3.4. Approximately 30% of runs converge to a sub-optimal local maximum corresponding to a side lobe in the Rabi oscillation pattern. This failure mode occurs when the initial stratified sampling by chance places no

points near the true global maximum, causing the surrogate to misidentify a side lobe as the primary peak.

Importantly, the bimodality demonstrates why the basin-hopping acquisition strategy (§3.4) is necessary: without forced exploration of distant basins, the optimizer would prematurely exploit the nearest local maximum. The 70% success rate for q1 represents the fraction of runs where basin-hopping successfully discovered the true global optimum by sampling the “High” basin when initial convergence favored the “Low” basin.

Intermediate performance (q4): Qubit q4 exhibits median error $\sim 2 \times 10^{-3}$ with occasional outliers reaching 10^{-2} . The broader error distribution compared to q0/q2/q3 suggests either: (1) a more complex Rabi landscape with multiple competing local maxima, (2) stronger crosstalk interactions requiring more careful utility balancing, or (3) higher measurement noise during the data collection phase for this particular qubit.

Overall success rate: Across all 5 qubits and 250 total optimization runs, the method achieves $>85\%$ success rate for errors $< 10^{-2}$, confirming reliable performance suitable for production quantum systems. The seed-to-seed variability underscores the importance of robust initialization strategies and adaptive acquisition functions that can recover from poor initial samples.

D. Crosstalk Penalty Validation

A specific focus of the evaluation is the optimizer’s ability to navigate the “Crosstalk Trap”—situations where maximizing target qubit response inadvertently causes strong off-target excitation of neighboring qubits.

In regimes where the crosstalk penalty weight $\lambda > 0$ (see Eq. 3 in §3.1), the peak of the drive response often does not align with the peak of the total utility [7]. A naive optimizer might maximize qubit excitation while ignoring collisions with spectator qubits, leading to reduced two-qubit gate fidelities or even logical errors in multi-qubit circuits.

We evaluate this by tracking the optimizer’s trajectory in the Z_{drive} vs. Z_{xtalk} plane during training. Successful convergence is characterized by the agent settling on the Pareto-optimal front where further increases in drive utility would incur unacceptable crosstalk penalties. Our results (not shown explicitly in figures due to space constraints) confirm that the utility-based acquisition function correctly balances these competing objectives, selecting amplitudes that achieve $>95\%$ of maximum drive utility while maintaining crosstalk below empirically determined thresholds.

This validation demonstrates that the method naturally extends to ensemble calibration scenarios where multiple qubits must be tuned simultaneously under shared coupling constraints [15], rather than requiring pairwise sequential calibration that scales poorly to large systems.

VII. DISCUSSION

A. Contributions

This work represents the first approach to calibrate superconducting qubits as an ensemble system [9], [15]. The demonstrated amplitude optimization provides a foundation for more comprehensive calibration schemes that can navigate the complex parameter landscape where changing one qubit's settings affects others.

B. Limitations

The current implementation focuses exclusively on amplitude learning and does not yet address phase calibration, which also matters for achieving high gate fidelity in superconducting qubit control. Several extensions would enhance the practical applicability of this approach:

- 1) Consider phase in the model as well
- 2) Handle more complicated drive waveforms beyond simple amplitude modulation
- 3) Adjust z-scores to be relative to zero-amplitude pulse baseline measurements
- 4) Implement reinforcement learning for control loop decisions [16], specifically determining when to take baseline measurements and when to explore new amplitudes

VIII. CONCLUSION

In this report, we present a method of tuning drive pulse amplitude of transmon qubits while minimizing the number of measurements taken by leveraging multi-layer perceptron surrogates [10]. A Bayesian optimization framework [5] is implemented with the MLP surrogates being utilized to propose the next drive amplitude to measure. This method converges to the same drive amplitudes as an exhaustive search with 32% fewer measurements, while remaining scalable to multi-dimensional optimization.

The key learning experience from this work is the practical demonstration that Bayesian optimization with compact neural surrogates can achieve sample-efficient calibration on real quantum hardware. The tight integration between data collection, surrogate training, and acquisition strategy proved essential for robust performance.

Several promising directions remain for future work: (1) extending the method to simultaneous multi-parameter optimization (amplitude, phase, frequency, duration), (2) implementing real-time drift compensation by continuously updating the surrogate during long calibration sessions, (3) scaling the approach to 10+ qubit systems with more complex crosstalk patterns, (4) integrating the calibration framework with quantum error correction protocols that require frequent recalibration, and (5) exploring transfer learning techniques to leverage calibration data across similar quantum processors.

CODE AND DATA AVAILABILITY

The complete dataset and analysis scripts are available upon request. Full experimental parameters and hyperparameters are documented in configuration files to ensure reproducibility.

ACKNOWLEDGMENT

This is a course project report for ECSE 6560 Modern Communication Systems. We thank Dr. Zhiding Liang for guidance on quantum computing research and for providing access to the Qolab quantum hardware via the IQCC Cloud platform. Claude AI was used to proofread and enhance writing; however, all technical content, analysis, and experimental work are original contributions by the authors. Hisen Zhang conducted background research, literature review, real quantum computer interfacing, and dataset creation. Dan Fiumara designed, implemented, and evaluated the machine learning pipeline and performed additional analysis.

REFERENCES

- [1] J. C. Bardin, D. H. Slichter, and D. J. Reilly, "Microwaves in Quantum Computing," *IEEE Journal of Microwaves*, vol. 1, no. 1, pp. 403–427, Jan. 2021.
- [2] P. Krantz, M. Kjaergaard, F. Yan, T. P. Orlando, S. Gustavsson, and W. D. Oliver, "A Quantum Engineer's Guide to Superconducting Qubits," *Applied Physics Reviews*, vol. 6, no. 2, p. 021318, Jun. 2019.
- [3] J. Koch et al., "Charge-insensitive qubit design derived from the Cooper pair box," *Physical Review A*, vol. 76, no. 4, p. 042319, Oct. 2007.
- [4] A. P. M. Place, L. V. H. Rodgers, P. Mundada, B. M. Smitham, M. Fitzpatrick, Z. Leng, A. Premkumar, J. Bryon, A. Vrajitoarea, S. Sussman, G. Cheng, T. Madhavan, H. K. Babla, X. H. Le, Y. Gang, B. Jäck, A. Gynis, N. Yao, R. J. Cava, N. P. de Leon, and A. A. Houck, "New material platform for superconducting transmon qubits with coherence times exceeding 0.3 milliseconds," *Nature Communications*, vol. 12, no. 1, p. 1779, Mar. 2021.
- [5] C. L. Cortes, P. Lefebvre, N. Lauk, M. J. Davis, N. Sinclair, S. K. Gray, and D. Oblak, "Sample-Efficient Adaptive Calibration of Quantum Networks Using Bayesian Optimization," *Physical Review Applied*, vol. 17, no. 3, p. 034067, Mar. 2022.
- [6] P. Qian, S. Qamar, X. Xiao, Y. Gu, X. Chai, Z. Zhao, N. Forcellini, and D. E. Liu, "Fast Quantum Calibration using Bayesian Optimization with State Parameter Estimator for Non-Markovian Environment," arXiv:2205.12929, May 2022.
- [7] A. Ketterer and T. Wellens, "Characterizing crosstalk of superconducting transmon processors," *Physical Review Applied*, vol. 20, no. 3, p. 034065, Sep. 2023.
- [8] S. Sheldon, L. S. Bishop, E. Magesan, S. Filipp, J. M. Chow, and J. M. Gambetta, "High-Speed Calibration and Characterization of Superconducting Quantum Processors without Qubit Reset," *PRX Quantum*, vol. 2, no. 2, p. 020324, May 2021.
- [9] É. Genois, J. A. Gross, A. Di Paolo, N. J. Stevenson, G. Koolstra, A. Hashim, I. Siddiqi, and A. Blais, "Quantum-tailored machine-learning characterization of a superconducting qubit," *PRX Quantum*, vol. 2, no. 4, p. 040355, Dec. 2021.
- [10] Y. L. Li, T. G. J. Rudner, and A. G. Wilson, "A Study of Bayesian Neural Network Surrogates for Bayesian Optimization," arXiv:2305.20028, May 2024.
- [11] Y. Wang, X. Zou, and Y. Wu, "Deep neural network-based surrogate-assisted evolutionary algorithm for expensive constrained optimization," *Cluster Computing*, vol. 28, p. 565, Aug. 2025.
- [12] A. A. Saki et al., "Low Crosstalk in a Scalable Superconducting Quantum Lattice," arXiv:2505.22276, May 2025.
- [13] F. Lange et al., "Cross-talk in superconducting qubit lattices with tunable couplers—comparing transmon and fluxonium architectures," arXiv:2504.10298, Dec. 2025.
- [14] S. Wang et al., "Characterizing and Mitigating Flux Crosstalk in Superconducting Qubits-Couplers System," arXiv:2508.03434, Oct. 2025.
- [15] Y. Wu et al., "Qubit Health Analytics and Clustering for HPC-Integrated Quantum Processors," arXiv:2508.21231, Aug. 2025.
- [16] X. Zhang et al., "Superconducting quantum computing optimization based on multi-objective deep reinforcement learning," *Scientific Reports*, vol. 14, p. 24255, Jan. 2025.